4.1 Introduction

AlN is a compound with a hexagonal close packed [wurtzite hcp] crystallographic structure and has a density of 3.262 g.cm^{-3} [35]. Its lattice parameters a and c are 0.311 and 0.4975 nm respectively[36] while the ratio c/a = 1.599. Probably due to a high nucleation barrier of the AlN-hcp lattice phase, it has been reported that AlN nucleates first with a metastable coherent fcc crystallographic structure that transforms later to the stable incoherent hcp crystallographic structure[37,38]. Wever et al[39] observed that the nitride was of the form Al-X-N where X could be oxygen, carbon or iron and Kang et al[37] observed that the nitride was of the form [Al, Cr]N. However the mechanism by which the nitride Al-X-N transforms to the stable hcp AlN has not been clearly identified, that is, whether the AlN forms after dissolution of the intermediate [Al, Cr]N or the latter transforms to the hcp AlN by local atomic migration, with Cr being rejected into the matrix.

4.2 The equilibrium solubility of AlN in steel

The solubility of AlN in steel conforms to the normal solubility product equation given by:

$$Log[\%M][\%X] = A - \left(\frac{B}{T}\right) \qquad (4.1)$$

$$Log[\%M]^{a/b}[\%X] = A' - \left(\frac{B'}{T}\right) \qquad (4.2)$$

where [%M] and [%X] represent the acid soluble aluminium (i.e. excluding Al bound up in alumina inclusions) and nitrogen contents respectively in wt% , T is the absolute temperature in K and A and B are constants.

The free energy of solution $\triangle H$ is given by[40]:

$$\Delta H = 1.15RA \tag{4.3}$$

or for equation 4.2:

$$\Delta H = 2.3RA\left(\frac{b}{a+b}\right) \tag{4.4}$$

where R is the universal gas constant, a and b are the valences for X and M respectively.

The solubility limit equations of AlN in austenite and ferrite have been obtained by a number of authors and are given in the appendix. The differences in these equations probably arose from the different techniques that were used to determine those solubility equations. For instance Darken et al[41] used the equilibrium Sieverts method that is based on the solubility of gasses in metals and their dependence on the applied pressure, i.e.

$$N_{gas} = k\sqrt{p} \tag{4.5}$$

where N_{gas} is the solubility of the dissolved gas, p is the pressure and k is a constant.

The solubility limit is established by measuring the point of departure from Sieverts' law at constant temperature. Sieverts' method generally gives higher solubility limit values compared to the Beeghly method (see below).

Most workers[41-48] used the Beeghly analysis[53] in which the iron matrix is dissolved in an ester-halogen solution (bromide-methyl acetate) and the insoluble nitrides are sieved/filtered. The limitations with this method are firstly, that it does not reliably distinguish AlN from other nitrides e.g. TiN, CrN and Si_3N_4 and secondly, it is insensitive to finer precipitates (< 10 nm) which could pass through the filter[42]. The latter effect would tend to lower the predicted solubility limit. As a result a reduced solubility is then reported when compared to the methods based on the Sieverts equation.

4.3 The precipitation of AlN in Al-killed low carbon steels

The chemical driving force for the nucleation of AlN is governed by the aluminium and nitrogen supersaturation, which is determined by the steel composition. The chemical driving force ΔG_V and the activation energy for nucleation ΔG^* are given by equations 3.4 and 3.6 respectively. The rate of isothermal nucleation is given by equation 3.16.

The rate of AlN precipitation is mainly controlled by the chemical driving force for nucleation, the interfacial energy and the mobility of aluminium atoms in ferrite or austenite. The diffusion of aluminium and nitrogen in austenite are given as [54,55]:

$$D_{Al} = 5.9\exp\left(-\frac{241000}{RT}\right) \quad (\text{cm}^2\ \text{s}^{-1}) \qquad (4.6)$$

$$D_N = 4.88x10^{-3}\exp\left(-\frac{76780}{RT}\right) \quad (\text{cm}^2\ \text{s}^{-1}) \qquad (4.7)$$

Due to the high diffusivity of nitrogen, it is generally assumed that no nitrogen concentration gradient will occur during particle growth and, therefore, the diffusion of aluminium atoms is likely to be the rate controlling species in the precipitation of AlN. Therefore, the parameter Zβ would be given as[56]:

$$Z\beta = D_{Al}(X_{Al}^{\ o} - X_{Al}^{\ equ})\left(\frac{F}{a^3}\right) \qquad (4.8)$$

where D_{Al} is the diffusion coefficient of aluminium, X_{Al}^{o} is the actual concentration in the matrix and X_{Al}^{equ} is the thermodynamic equilibrium concentration of solute aluminium, F is the number of atoms per unit cell (FCC = 4) and a is the lattice parameter.

If nucleation occurs heterogeneously on dislocations, the parameter N_o in equation 3.15 is given by[57,58]:

$$N_o = 0.5\rho^{1.5} \tag{4.9}$$

where ρ is the dislocation density at the start of precipitation.

Typical TTT diagrams for the precipitation of AlN in austenite and ferrite are given in figures 4.1 and 4.2. As may be seen in figure 4.1, the onset of the austenite to ferrite phase change has a significant accelerating effect on the precipitation of AlN due to the higher diffusivity of aluminium in ferrite and a decreased solubility of AlN in ferrite. At 800 °C and in ferrite, AlN precipitates almost without an incubation time at the estimated nose of the TTT diagram, see figure 4.2 below.

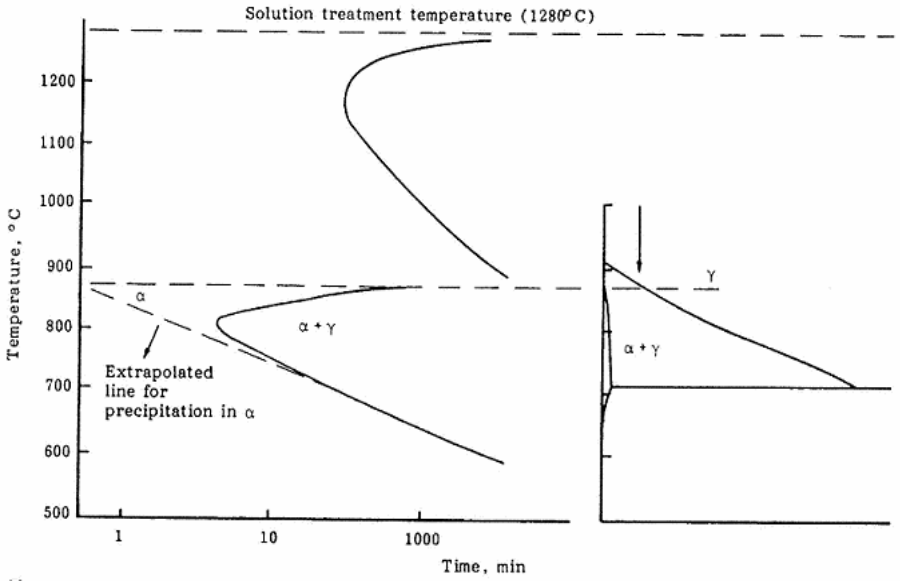

Figure 4.1: The time required for 50% precipitation of AlN, showing the pronounced effect of the austenite to ferrite phase change in Fe-0.05C-0.3Mn-0.12Al-0.007N, from Mayrhofer et al[47].

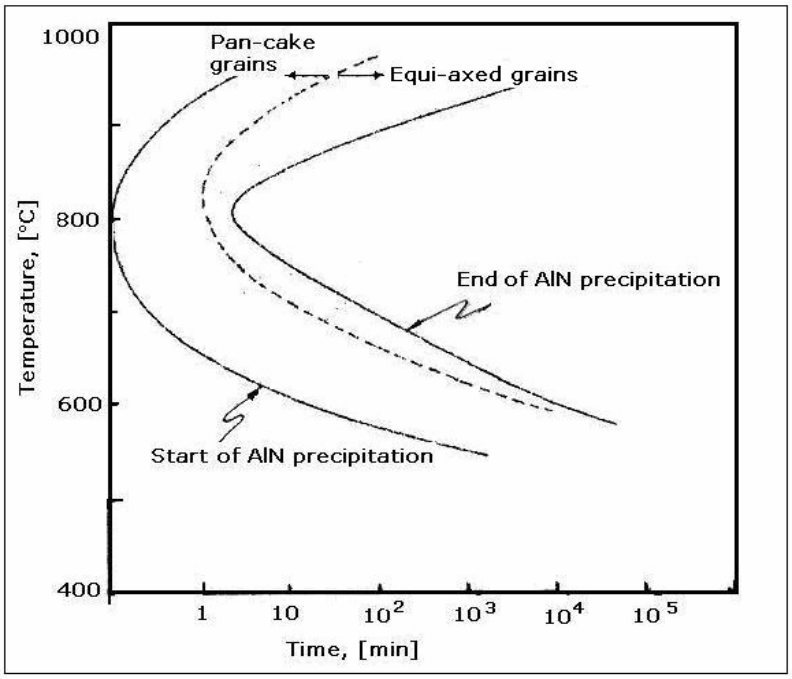

Figure 4.2: The TTT diagram for AlN precipitation in a low carbon Al-killed steel hot band[65]

In recent studies[52,59,60] done on commercial Al-killed low carbon steels, it was observed that the AlN precipitation in austenite took place at earlier times contrary to what is shown in figure 4.1. The AlN reportedly precipitated during hot rolling above the A_{r3} temperature and nucleated heterogeneously on MnS particles. Engl et al[60] observed heterogeneous nucleation of AlN on MnS during coiling of low carbon Al-killed steels within the temperature range of 600 °C to 800 °C. The AlN nucleated heterogeneously with ease on the MnS particles as the latter reduced the nucleation barrier of the former.

During re-austenitisation of low carbon-manganese Al-killed steels, freshly precipitated AlN grows according to the relationship[11]:

$$Log\left(r\right)=2.593+\frac{\log\left(t\right)}{3}-\frac{5167}{T} \qquad (4.10)$$

where r is the mean particle radius (μm), t is the isothermal holding time (hr) and T is the absolute temperature (K).

In the same steels, the following relationship was found in ferrite[155]:

$$Log\left(r_t-r_o\right)=12.3+0.85\log(t)-\frac{14433}{T} \qquad (4.11)$$

while in 50 percent deformed ferrite the following relationship was found:

$$Log\left(r_t-r_o\right)=16.4+0.85\log(t)-\frac{14433}{T} \qquad (4.12)$$

where r_t is the mean particle radius (nm) at time t (min), r_o is the initial mean particle radius and T is the absolute temperature (K).

4.4 Crystallographic orientation relationship between AlN and the iron matrix

Work has been done on the orientation relationship between the bcc and fcc iron matrix and the fcc and hcp AlN. Cheng et al[68] observed the following orientation relationship between the fcc iron matrix and the hcp AlN:

$$\left[0\bar{1}\bar{1}0\right]_{AlN} // \left[\bar{1}\bar{1}2\right]_{fcc-Fe}$$

$$\left(0001\right)_{AlN} // \left(1\bar{1}\bar{1}\right)_{fcc-Fe}$$

$$\left(2\bar{1}\bar{1}0\right)_{AlN} // \left(110\right)_{fcc-Fe}$$

while Sennour et al[38] and Massardier et al[69] observed a Bain orientation relationship between the cubic (NaCl type) structure and the bcc iron matrix:

$$\left(001\right)_{AlN} // \left(100\right)_{bcc-Fe}$$

$$\left[110\right]_{AlN} // \left[001\right]_{bcc-Fe}$$

The following orientation was also observed between the hcp AlN and the ferrite matrix[38]:

$$\left(03\bar{3}4\right)_{AlN} // \left(110\right)_{bcc-Fe}$$

$$\left[2\bar{1}\bar{1}0\right]_{AlN} // \left[2\bar{2}\bar{3}\right]_{bcc-Fe}$$

The orientation relationship between the hcp AlN and the fcc MnS was found to be as follows[52]:

$$\left(0001\right)_{AlN} // \left(1\bar{1}1\right)_{MnS}$$

$$\left[10\bar{1}0\right]_{AlN} // \left[121\right]_{MnS}$$

$$\left[2\bar{1}\bar{1}0\right]_{AlN} // \left[110\right]_{MnS}$$

As may be seen, the orientation relationship between the hcp AlN and the fcc MnS is the same as that between hcp AlN and fcc Fe. It is also worthwhile mentioning that both electron energy loss spectroscopy [EELS] and the energy dispersive X-ray [EDX] micro-analyses revealed the stoichiometric Al and N composition of the AlN[38].

4.5 The dissolution of AlN during reheating

As may be seen from the solubility models in the appendix, it is predicted that the equilibrium solubility of AlN in steels is not affected by other alloying elements. Mayrhofer et al[47] established that even in the presence of coarse AlN, equilibrium was attained within minutes (< 10 min) at temperatures above 1000 °C. This implies that during austenitisation under industrial processing conditions, the equilibrium dissolution of AlN is easily attained regardless of the process route whether it is the cold charge or hot charge route.

Chapter 5 The precipitation of manganese sulphide [MnS] in steels

5.1 Introduction

Sulphur may be present in steel in solute atom or sulphide form. Sulphides in steel generally comprise one or more of the phases, FeS, MnS, CuS and CaS. Frequently there can be extensive solid solution of other elements in the sulphide[61]. However, MnS is the normal form of sulphide in many steels. MnS (alabandite) has an fcc crystallographic structure and the lattice parameter is 0.5222 nm [62]. Depending on the Mn to S ratio of the steel and the cooling rate, it can contain variable amounts of FeS. Diffusion may then occur during subsequent reheating to produce "pure" MnS, which is virtually free from iron.

The morphology of the MnS in as-cast steel depends on the degree of deoxidation of the melt. In general as the degree of deoxidation increases the morphology changes from the globular through dendritic (branched rods) to the angular type[63,64]. MnS is readily deformed during hot rolling and, therefore, it changes its morphology to string-type or even plate-like which adversely affects the mechanical properties of the steel. Therefore, generally, calcium or rare earths such as cerium are added for shape control of the sulphides.

5.2 The solubility of MnS in low carbon steels

The equilibrium solubility of MnS in steel conforms to the normal solubility product of equation 4.1. The equilibrium solubility limit of MnS in austenite obtained by different workers is given in Table 5.1.

Chapter 5 The precipitation of manganese sulphide [MnS] in steels

Table 5.1: The equilibrium solubility limit of MnS in austenite.

Solubility model: Log[%Mn][%S]	Ref
$2.929-\left(\frac{9020}{T}\right)$	Turkdogan et al[65]
$10.6-\left(\frac{19427}{T}\right)$	Leslie et al[66]
$5.02-\left(\frac{11625}{T}\right)$	Parks et al[162]

5.3 The precipitation kinetics MnS in low carbon steels

Depending on the cooling rate and the Mn to S ratio in the steel, the Mn and S can either exist as solute atoms or precipitates in the steel. The re-precipitation of the sulphides in a low carbon steel (Fe - 0.11-0.14C - 0.6Mn - 0.25Si - 0.22Cr - 0.025-0.037S) was studied by Gabarz et al[67] and their TTT diagram is given in figure 5.1.

No pure MnS precipitates were observed; the EDS analysis showed that the MnS contained some Cu, probably due to the higher copper content in the steel. The dissolution temperatures

for each type of the sulphides were established to be about 1300 °C for MnS, 1100 to 1150 °C for [Mn,Cu]S and 950 °C for CuS and Cu_2S as shown in figure 5.1.

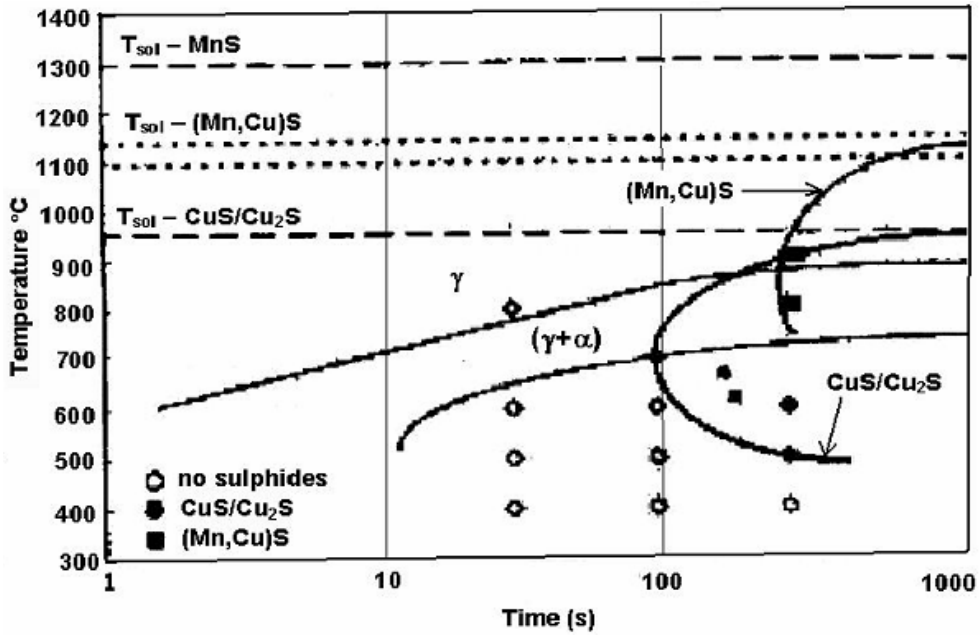

Figure 5.1: The re-precipitation start curves for nano-sulphides in a laboratory ingot. Note that no "pure" MnS was observed[67].

The MnS particle size and distribution depends on the cooling rate and the Mn to S ratio, which in turn affect the supersaturation and the nucleation and growth of the MnS particles. Apart from the Mn to S ratio, the thermal history plays an important role in the thermokinetics of the precipitation of the MnS. For instance, in a previous study on a low carbon high sulphur steel (Fe-0.04C-0.25Mn-0.2Si-0.005Al-0.0026N- 0.005-0.04S), Frawley et al[68] observed that the particle size and distribution of MnS in the Hot

Chapter 5 The precipitation of manganese sulphide [MnS] in steels

Charge Route (HCR) specimens were different from that in the Cold Charge Route (CCR) specimens, the former being a finer dispersion of MnS of 5 to 30 nm as a result of the higher supersaturation, and the latter a combination of finer and larger ones, 100 to 200 nm in size. The two populations in the CCR specimens were believed to be a result of the partial dissolution of the MnS during the reheating process. In previous studies[67,71], it was observed that during hot rolling, MnS generally precipitated heterogeneously on the grain boundaries and dislocations, more than inside the grains themselves.

In steels that contain substantial amounts of copper due to higher scrap steel recycling, the MnS is mostly associated with copper. As the MnS forms at a higher temperature, Madariaga et al[72] found that the hcp CuS (covellite), with parameters a = 0.379 nm and c = 1.633 nm, formed a shell around the MnS. It was suggested that the lowest misfit orientation of 6% (calculated from the Bramfitt[73] equation) existed between the CuS and the ferrite matrix:

$$(0001)_{CuS} // (111)_{bcc-Fe}$$

$$\left[2\bar{1}\bar{1}0\right]_{CuS} // \left[1\bar{1}0\right]_{bcc-Fe}$$

Liu et al[74] also observed a [Cu, Fe]S shell around the MnS particles by EDS analysis. Fine fcc Cu_2S particles, (diginite), < 50

nm with the lattice parameter a = 0.5735 nm, were observed as well. The cube-cube orientation relationship between this precipitate and the matrix was observed to be:

$$(001)_{Cu_2S} // (001)_{bcc-Fe}$$

$$[110]_{Cu_2S} // [110]_{bcc-Fe}$$

Chapter 6 The theory of recovery and recrystallisation in metals

6.1 Introduction

When a metal is subjected to plastic deformation by cold work, most of the energy in the deformation process is converted into heat and the remainder is stored in the metal. It is this stored energy that provides the driving force for either recovery or recrystallisation during the annealing process, i.e. in the deformed state the material is thermodynamically unstable and upon increasing the temperature to generally near to or above half of the melting temperature [$0.5T_m$], the material lowers its free energy ΔG by the reduction in number and rearrangement of the lattice defects. Detailed reviews of this subject have been done by different authors over the years[75-78].

Recovery embraces all of the earliest structural and property changes that do not involve the sweeping of the deformed structure by migrating high angle grain boundaries. The deformed structure thus retains its identity while the density of crystal defects and their distribution changes. This involves annealing of point defects, annihilation and rearrangement of dislocations, formation of sub-grains (polygonisation) and their subsequent growth that leads to the formation of recrystallisation nuclei.

Recrystallisation takes place by the nucleation and growth of new grains. The nucleation stage involves the formation of a small volume of relatively dislocation free material which is at least partially bound by a high angle grain boundary within the deformed material. In order to be viable a nucleus, this volume of

material must be of sufficient size to be able to grow into the deformed material. In the case of the Strain Induced Boundary Migration mechanism, what is perceived as an "incubation time" actually involves the early development of the pre-existing recrystallisation interfaces (pre-existing high angle grain boundaries). This early development stage involves the initial migration of the high angle grain boundaries into the deformed material to a hemi-spherical size, which is a critical nucleus size for full recrystallisation to proceed. Further annealing after recrystallisation causes the grains to grow larger in size through grain growth. As mentioned earlier, there is no distinct demarcation between these processes and, therefore, grain growth, which has no incubation time, may start before the completion of the recrystallisation process, depending on the prevailing local conditions in the material.

6.2 Kinetics of recovery

The rate of property change is highest at the start of the annealing process and gradually decreases as recovery progresses. At longer times the rate of property change becomes negligible. The kinetics of recovery in metals has been investigated as a function of time through the release of stored energy, the decrease in electrical resistance, the change in magnetic properties and x-ray line broadening[79-82]. Unlike recrystallisation, there is no incubation period for the recovery process.

Chapter 6 The theory of recovery and recrystallisation in metals

The temperature dependence of the rate of recovery is generally of the Arrhenius type i.e. for the rate of change of any property X:

$$\frac{dX}{dt} \; or \; \frac{C_1}{t} = C\exp\left(-\frac{Q}{RT}\right) \qquad (6.1)$$

where C_1 is some constant representing a fixed percentage of recrystallisation within the linear portion of the property X versus time t curve, C is the frequency factor (a combination of the vibration frequency and the entropy term), Q is the activation energy in J mol^{-1} for the process, R is the universal gas constant (8.314 J mol^{-1} K^{-1}) and T is the absolute temperature in K.

By taking logs on both sides of equation 6.1, it becomes:

$$\ln\left(\frac{1}{t}\right) = \ln C_2 - \left(\frac{Q}{RT}\right) \qquad (6.2)$$

where $\ln C_2 = (\ln C - \ln C_1)$

Thus, when the rate $\ln\left(\frac{1}{t}\right)$ is plotted versus $\frac{1}{T}$, the slope is $-\frac{Q}{R}$ and this gives the activation energy of the process.

There is a tendency for equation 6.2 to deviate from linearity as recovery progresses and Kuhlmann et al[83] assumed that the instantaneous rate of recovery depends on the extent of recovery according to the expression:

$$\frac{dX}{dt} = C_3 X.\exp\left[-\frac{(Q - mX)}{RT}\right] \qquad (6.3)$$

where X is the quantity of the measured property that has departed from equilibrium at time t, while C_3 and m are constants.

The activation energy for recovery then increases linearly with the increase in recovery. Li et al[84] made similar observations that the activation energy for recovery should be a linear function of the extent of recovery.

6.3 Recrystallisation Kinetics

The kinetics of recrystallisation can be followed successfully, in most cases, by applying the MAJK (Kolmogorov[85] Johnson-Mehl[86] and Avrami[87]) equation also known as the Avrami equation. This equation is based on a sigmoidal relationship between the recrystallised volume fraction X and the isothermal annealing time t that is found often.

The problem of relating the volume fraction recrystallised X to the annealing time t is complicated by the situation that as recrystallisation proceeds, the volume of unrecrystallised material into which the new nuclei can form keeps on diminishing. In order to circumvent this complication, Johnson et al[86] introduced the concept of an "extended volume" that takes into account the

impingement of grains on each other as recrystallisation proceeds. The general MAJK expression that predicts the volume fraction of the material recrystallised X in time t is then given by:

$$X = 1 - \exp\left(-kt^{n}\right) \qquad (6.4)$$

where n is the Avrami exponent and k comprises the shape factor *f*, the nucleation frequency Ṅ and the growth rate *G*.

It is generally assumed that the nucleation sites are randomly distributed in the deformed matrix, that the growth is isotropic and that the growth rate is constant. If the nucleation rate Ṅ remains constant, [Johnson-Mehl nucleation kinetics] then n = 4. If all the nuclei are present at time zero and no further nucleation takes place afterwards, i.e. "site saturation" has occurred, n = 3.

In order to determine the exponent n and the parameter k, it is customary to plot $\ln\left\{\ln\left(\frac{1}{1-X}\right)\right\}$ versus ln(t). The plot is usually a straight line of slope n and with k the intercept. Factors that contribute to deviation from linearity are discussed in the following section 6.4.

Another way of studying the kinetics of the recrystallisation process is to measure the time $t_{0.5}$ taken for the 50 percent recrystallised volume fraction to be reached during the isothermal annealing process. This assumes that nucleation has stopped before 50 percent recrystallisation i.e. Ṅ = 0, (site saturation)

and that the extent of recrystallised volume fraction is governed solely by the growth rate G.

The effect of increasing the annealing temperature T, is the reduction in the time $t_{0.5}$ taken to recrystallise to 50 percent volume fraction. When the reciprocal of the annealing temperature is plotted versus the logarithm of the annealing time for the 50 percent recrystallisation, a straight line is obtained i.e.:

$$t_{0.5} = C_4 \exp\left(\frac{Q_r}{RT}\right) \tag{6.5}$$

where C_4 is a parameter that is structure dependent and Q_r is the apparent activation energy for recrystallisation. Q_r is an "apparent" activation energy because there is generally an overlap between recovery, recrystallisation and grain growth during the annealing process.

6.4 The Avrami exponent n

The assumptions of constant nucleation $\dot{N}$ and growth rate G in the derivation of the MAJK equation are seldom achieved in practice. It is quite usual for both to vary with time during annealing and, therefore, the $\ln\left[\ln\left(\frac{1}{1-X}\right)\right]$ versus ln(t) plot is not always linear[88,89]. For many materials, the experimentally determined JMAK exponent does not only vary as the recrystallisation progresses but is generally smaller than predicted by the ideal JMAK model. Significantly smaller JMAK exponents

are obtained in the later stages of recrystallisation due to the diminishing driving force in the deformed matrix caused by concurrent or preceding recovery. The implication is that a constant exponent n may overestimate the recrystallisation kinetics in the later stages of the annealing process. The extent of recovery is dependent on the type of material (i.e. materials with a high stacking fault energy recover easier), annealing temperature, amount of deformation and the heating rate (in the case of a continuous annealing process).

The deviation from the ideal MAJK behaviour is also attributed to non-uniform distribution of the stored energy of deformation, non-random distribution of nuclei, anisotropic growth of recrystallised nuclei and sometimes the presence of second phase particles[88,90-92]. In spite of these deficiencies, the MAJK equation is still widely used in the study of the kinetics of recrystallisation in materials.

6.5 Nucleation in recrystallisation

Nucleation during recrystallisation involves the formation of a small volume of relatively dislocation-free material, which is partly bound by a high angle grain boundary that is capable of migrating within the deformed material. The mechanisms for the nucleation of the recrystallisation can be classified into basically three models, namely classical nucleation through an embryo, the Strain Induced Boundary Migration (SIBM) and the subgrain coalescence and rotation models.

Chapter 6 The theory of recovery and recrystallisation in metals

In a recent publication in which the nucleation of recrystallisation is reviewed, Humphreys[93], concluded that the main mechanisms are thought to involve the growth of subgrains by the migration of low angle boundaries in an orientation gradient or the strain induced boundary migration of existing boundaries. It was also concluded that to date, there is no firm experimental evidence that subgrain coalescence and rotation play a significant role in the nucleation of recrystallisation. As for classical nucleation through an embryo, it has been long recognised that new grains generally do not form by thermal fluctuation on an atom by atom basis as is the case in homogeneously nucleated solid state phase transformations, mainly due to rather low driving forces for nucleation of a stable recrystallised embryo. There is, furthermore, adequate evidence that recrystallised grains do nucleate and grow from pre-existing volumes/embryos such as cells or subgrains in the deformed material[78,94,95].

6.5.1 Classical nucleation theory

The application of classical nucleation theory to recrystallisation was first examined by Burke and Turnbull[91]. This may be a homogeneous or heterogeneous process with the latter nucleating at grain boundaries or other defects in the deformed matrix e.g. high deformation zones surrounding inclusions[92] as in Particle Stimulated Nucleation or PSN found in some aluminium alloys. It is to be noted, however, that in the PSN model, nucleation around inclusions is not a result of reduced retarding forces as in classical heterogeneous nucleation but is rather due to an increased driving

force present in the intensified deformation zones in these near-particle areas.

In the classical nucleation model where a potential spherical nucleus of recrystallised material is formed in the matrix, the free energy change is given by equation 3.3, where ΔG_v is the deformation energy or driving force in the matrix per unit volume, r is the radius of the nucleus and γ_{gb} is the grain boundary energy. The strain energy term ΔG_ε as a retarding force, is not included in equation 3.11 as there is no density difference between the deformed and undeformed matrix.

Here a critical nucleus will be stable if it reaches a critical size r* which is governed by the surface energy and the difference in deformation energy per unit volume between the recrystallised state and the deformed matrix, equation 3.3, while the activation energy in equation 3.6 is normally taken as the activation energy for grain boundary diffusion.

Contrary to Burke and Turnbull[91], Bailey[94] and Cahn[95] showed that homogeneous nucleation by the classical fluctuation mechanism is generally unlikely in recrystallisation due to the small driving forces and the high surface free energy of a high angle grain boundary. However, heterogeneous nucleation is a possibility since the critical energy to form a stable nucleus is reduced by a factor ξ [96]:

$$\xi = \frac{(2+\cos\theta)(1-\cos\theta)^2}{2} \qquad (6.6)$$

where θ is the is the included angle as shown in earlier figure 3.3.

Byrne et al[97] showed that theoretical calculations of the driving force and nucleation rate as a function of deformation showed that the classical theory of nucleation through formation of stable embryos on a pre-existing interface could possibly apply at deformations greater than 15 to 20 % where sufficient driving force will be available to form a measurable stable nucleus.

Classical nucleation theory predicts that the nucleus will form in such an orientation that the surface energy γ_s will be small in order to minimise this retarding force. This should, therefore, lead to a minimum critical radius r* and activation energy ΔG* through a good lattice fit of the nucleus and the matrix. One weakness with the classical nucleation theory is that in practice, the opposite is very often found because grain boundary mobility requires a high orientation difference between the new grain and the deformed matrix. For high angle grain boundaries (HAGB) in aluminium, Gottstein et al[98] suggested that, if the special 40°<111> tilt boundary is ignored, the grain boundary mobility M versus the misorientation θ curve is sigmoidal (see figure 6.1 below) with a form:

$$M = M_m\left[1-e^{-B(\theta/\theta_m)^n}\right] \qquad (6.7)$$

where M_m is the mobility of a high angle grain boundary, n ~ 4 and B ~ 5.

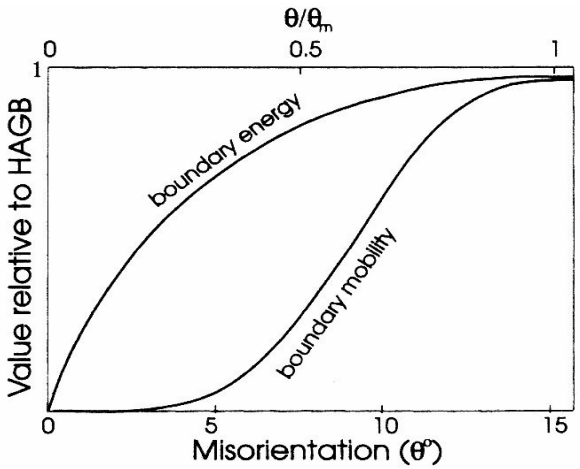

Figure 6.1: The variation in grain boundary energy and mobility with misorientation[98].

6.5.2 The Strain Induced Boundary Migration (SIBM) mechanism

Strain induced boundary migration was first reported by Beck and Sperry[99] (see figure 6.2 (a)) and the thermodynamics of the process was analysed by Bailey and Hirsch[100]. In this model, no formation of new embryos as stable nuclei is required. New grains grow from pre-existing nuclei present on grain boundaries by the sweeping up of the dislocations ahead of them by the interface moving into the deformed matrix. This model takes care of the constraint posed by the low driving forces for embryo formation through thermal fluctuations as proposed by the classical nucleation theory as no "stable nucleus" needs to be formed first.

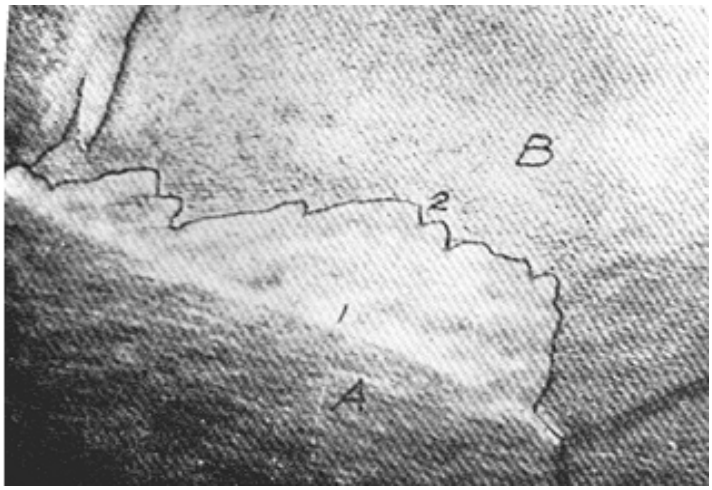

(a)

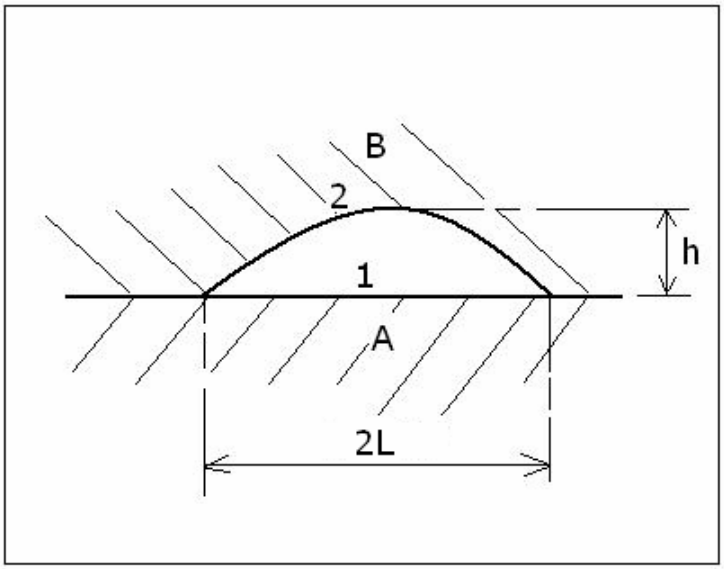

(b)

Figure 6.2: (a) Strain induced migration of a recrystallisation boundary[76] (b) schematic presentation of figure 6.2 (a).

The migrating grain boundary in figure 6.2 (a) is anchored at the two points on either side of the grain boundary portion that bulges out. The anchoring may be due to subgrain boundaries or pinning

by particles on the grain boundaries. In figure 6.2, the upper grain B has a higher dislocation density than the area between 1 and 2 so that the boundary tends to bulge out, as seen in the micrograph, in order to satisfy the local energy condition that balances the grain boundary interfacial energy γ_{gb} and the strain energy difference between the recrystallised grain and the deformed matrix (ΔG_{Rx}).

The rate of movement of the migrating front dh/dt is governed by the rate of net movement of atoms across the interface (boundary 2 in figure 6.2 above). Bailey et al[100] used the absolute reaction rate in this derivation i.e.:

$$\frac{dh}{dt} = \frac{2V_a^{1/3}\upsilon}{RT}\exp\left(-\frac{\Delta G_A}{RT}\right)\left[\left|\Delta G_{Rx}\right| - \left|\frac{\left(\gamma_{gb}4h\right)}{\left(L^2+h^2\right)}\right|\right] \quad (6.8)$$

where V_a is the volume of the migrating atoms, υ is their jump frequency, ΔG_A is the activation energy for the movement of the atoms across the interface, L and h are as shown in figure 6.2 (b) above, γ_{gb} is the grain boundary surface energy and the rest are as defined in the previous sections.

For growth to take place dh/dt > 0 and, therefore:

$$\left|\Delta G_{Rx}\right| > \left|\frac{\left(\gamma_{gb}4h\right)}{\left(L^2+h^2\right)}\right| \quad (6.9)$$

and with the maximum h = L i.e. for the subgrain to grow to a hemisphere and beyond:

$$\left|\Delta G_{Rx}\right| \geq \left|\frac{2\gamma_{gb}}{L}\right| \qquad (6.10)$$

The integration of equation 6.8 is complex and was examined schematically through inspection as shown in figure 6.3 below. The conclusion was that at low values of the driving force, i.e. $\Delta G_{Rx} < (2\gamma_{gb}/L)$, pre-existing embryos (pre-existing recrystallisation interfaces) will not grow into new full recrystallised grains. For full growth to take place at all values of h, $\Delta G_{Rx} > (2\gamma/L)$. It is also concluded that since no nucleation through thermally activated embryos is required, there should not be any incubation period as in the classical embryo/nucleus model. The extrapolation of the constant dh/dt portion of the curve in figure 6.4, however, gives an "apparent incubation" period which, according to the SIBM theory, is simply the time of slow growth in the early stages of the recrystallisation process.

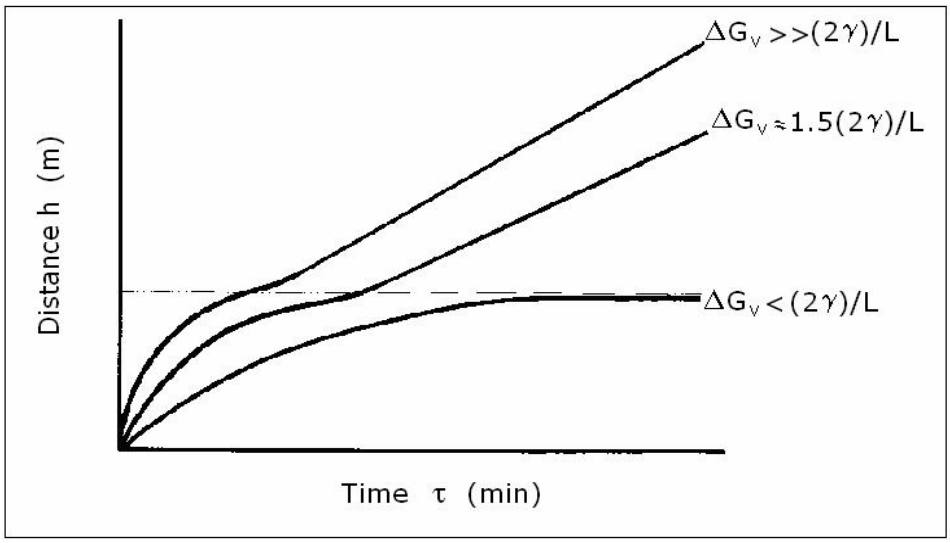

Figurer 6.3: Schematic rate of migration of the transformation front as a function of the driving force ΔG_{Rx}

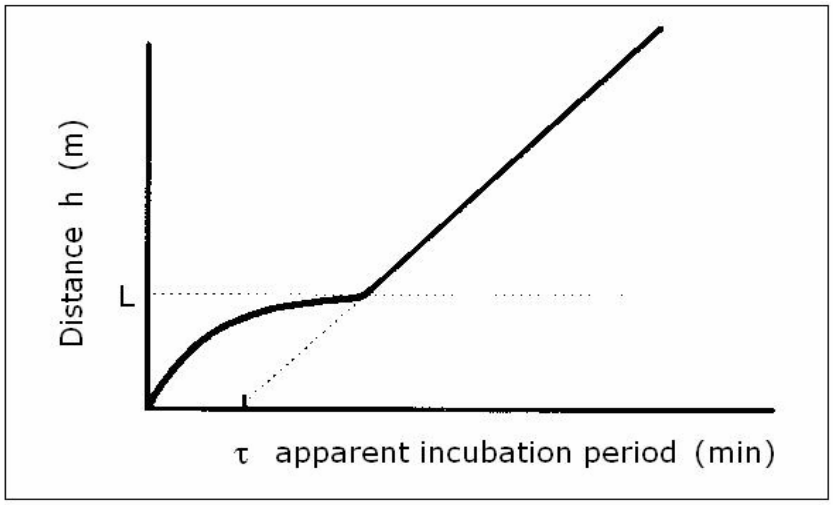

Figure 6.4: Apparent incubation time due to slow movement of the recrystallisation front at early stages of the recrystallisation process.

6.5.3 Subgrain coalescence and rotation

The mechanism proposed by Li requires that the subgrain coalescence and rotation of several subgrains lead into the formation of a potential embryo with a HAGB capable of growing into the deformed matrix[102,103] as illustrated in figure 6.5. The coalescence and rotation takes place through subgrain boundary diffusion. However, a number of authors[104,-106] have found no experimental evidence to substantiate this nucleation model.

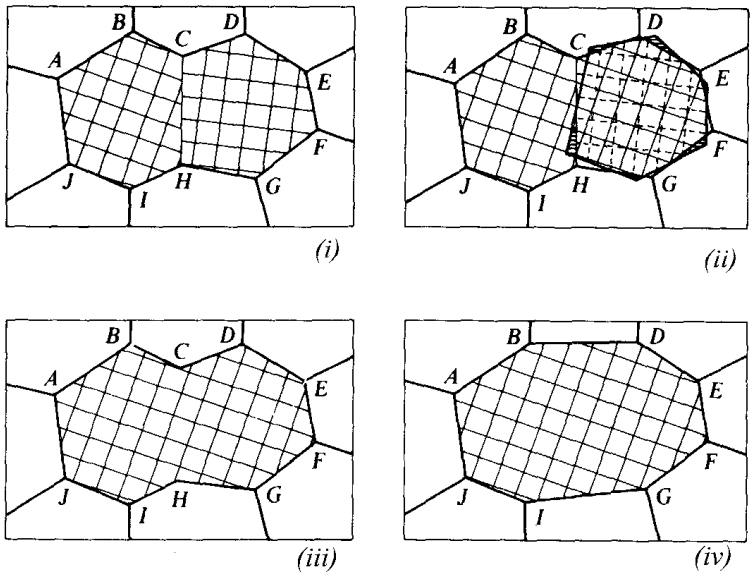

Figure 6.5: Schematic representation of subgrain rotation, leading to coalescence and an increase in orientation difference at the growth front. (i) Original subgrain structure before coalescence, (ii) Subgrain CDEFGH rotates through boundary diffusion (iii) The original orientation difference between the two subgrains has disappeared and the orientation difference at the front DEFG is now larger, (iv) Grain boundary sections BCD and IHG straighten out to achieve a lower energy state[102].

6.6 Effect of cold work on recrystallisation kinetics

Increasing the amount of deformation increases the amount of stored energy in the deformed matrix[79]. This stored energy is the driving force for the recrystallisation process and is given by:

$$P_d = \alpha G_m b^2 \Delta N_d \qquad (6.11)$$

where α is a constant with the value between 0.5 and 1.0, G_m is the shear modulus, b is the Burgers vector and ΔN_d is the difference in dislocation density between the deformed and the recrystallised state. However, $N_{d\text{-}\varepsilon} >> N_{d\text{-}Rx}$ so that $\Delta N_d \sim N_{d\text{-}\varepsilon}$; where $N_{d\text{-}\varepsilon}$ and $N_{d\text{-}RX}$ are the dislocation densities after cold work and recrystallisation respectively.

As a result, with increasing deformation recrystallisation will take place at earlier times during isothermal annealing, or at lower temperatures during isochronal annealing. The higher driving force resulting from the higher deformation (stored energy) decreases both the activation energies for nucleation and growth of the new grains[107], as found in aluminium, see figure 6.6.

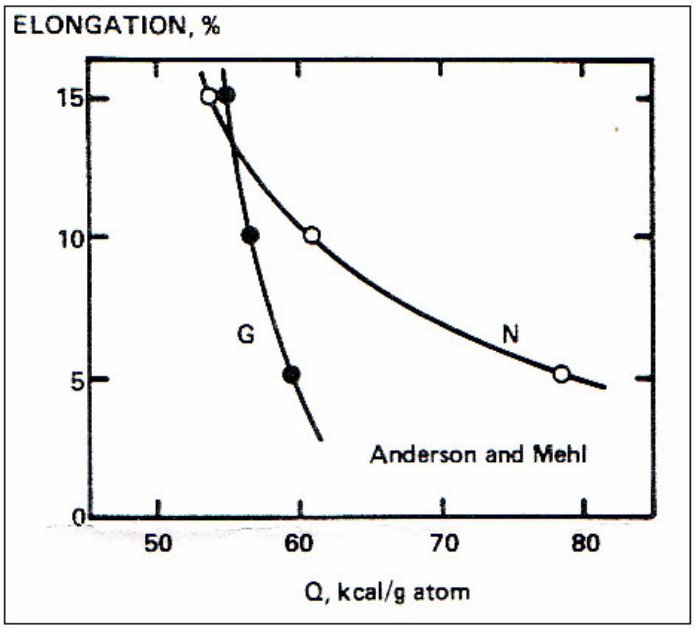

Figure 6.6: The activation energy for nucleation rate $\dot{N}$ and for growth rate G_R in aluminium as the function of the amount of deformation[107].

6.7 The effect of annealing temperature on the recrystallisation kinetics

Increasing the annealing temperature shifts the annealing time to earlier times, see figure 6.7 below, as recrystallisation is a thermally activated process and diffusion is faster at higher annealing temperatures. Apart from the driving force that arises from the stored deformation energy (equation 6.11), the grain boundary movement V_B of the new grains is also dependent on the grain boundary mobility m which is dependent on temperature, i.e. grain boundary mobility is higher at higher temperatures:

$$V_B = mP_{Rx} \tag{6.12}$$

$$m = m_o \exp\left[-\frac{Q_{gb}}{RT}\right] \tag{6.13}$$

where Q_{gb} is the activation energy for the grain boundary mobility.

As recovery and recrystallisation processes sometimes overlap, it is worthwhile mentioning that at lower annealing temperatures, recovery dominates over recrystallisation and, therefore, this reduces the driving force available for recrystallisation. In figure 6.7, the decrease in growth rate of new grains at later stages of recrystallisation was attributed to concurrent recovery at lower annealing temperatures[88].

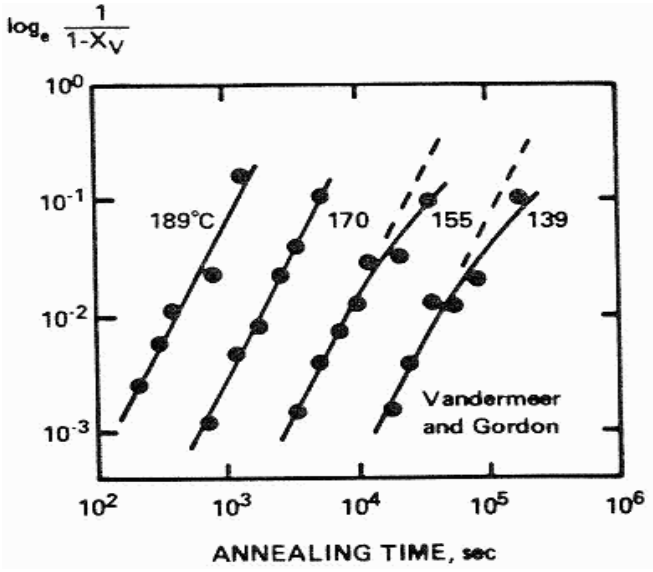

Figure 6.7: The effect of annealing temperature on the recrystallisation kinetics of a zone refined aluminium containing 6.8 ppm copper,

deformed 40% by rolling at 0°C then isothermally annealed at temperatures indicated: note that the recrystallisation process shifts to earlier times as the annealing temperature increases[88].

6.8 Effect of grain size on the recrystallisation kinetics

Indirectly, a smaller grain size may affect recrystallisation through a more intense work hardening process for a given deformation, thereby providing a higher driving force. In smaller grain size material, therefore, recrystallisation shifts to earlier annealing times during isothermal annealing and to lower temperatures during isochronal annealing because of the higher dislocation density[108]. Figure 6.8 shows the effect of grain size on the recrystallisation process of cold worked low carbon manganese steel.

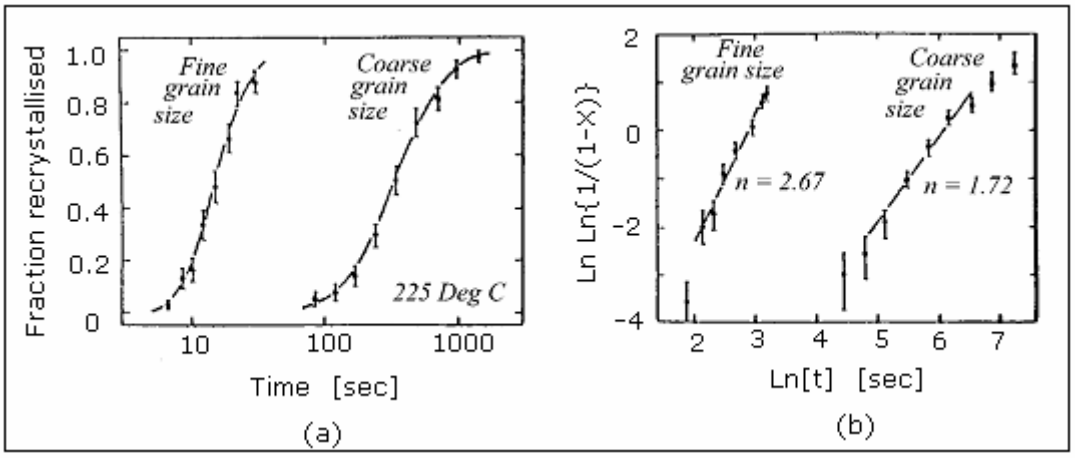

Figure 6.8: (a) Isothermal recrystallisation curves for pure Cu showing the effect of annealing at 225°C after cold work for a fine grained and

a coarse grained material and (b) the kinetics plotted according to the JMA equation. In both figures the vertical bars represent the 95 percent confidence limits. [108]

6.9 The influence of solutes and second phase particles on recrystallisation

The recrystallisation process in two-phase materials is usually quite complex. It is generally found that second phase particles may either retard or accelerate the recrystallisation process, if compared to an equivalent single phase material, depending on the conditions.

For instance, the presence of precipitates may affect the intensity and homogeneity of cold work during deformation. When an alloy is plastically deformed, the non-shearable particles will cause an increased dislocation density, thus increasing the driving force for subsequent recrystallisation, if compared to a single phase material. The regions around large particles may also act as preferred nucleation sites for recrystallisation due to inhomogeneous deformation (Particle Stimulated Nucleation PSN as has been found in aluminium alloys) while at the same time, small particles or closely spaced ones, may pin the grain boundaries and in effect limit their mobility. The dissolved elements (solute atoms and their clusters) can also affect the recrystallisation kinetics by segregating to dislocations, subgrain boundaries and grain boundaries with the result that their mobility is decreased by "impurity drag" or "solute drag".

Chapter 6 The theory of recovery and recrystallisation in metals

The situation becomes more complex as transformation processes of nucleation and growth or transformation of the precipitates to a more stable state and recrystallisation take place simultaneously or sequentially. In the case where semi-coherent precipitates transform to a stable incoherent state, followed by coarsening, an extra driving force is provided in the process as the system energy is lowered further and this promotes continuous recrystallisation[79]. Coarse particles may form in the rolling microbands whereas the metastable precipitates may form along side the microbands and this may lead to an evolution of banded recrystallised microstructures of coarser and finer grains respectively[78,109-112].

The interaction of particles with the grain or subgrain boundaries is generally explained by the Zener "drag" effect[113]. When a grain boundary migrates into a field of spherical incoherent particles of concentration n per unit volume of a mean radius r (whose interfacial energy γ_s is unchanged by the passage of a high angle grain boundary), the reduction in driving force per unit volume (also called the "pinning force") is, therefore, given by:

$$P_Z = \left(\frac{3\gamma_s}{4}\right)\left(\frac{V_v}{r}\right) \qquad (6.14)$$

Equation 6.14 indicates that finer precipitates and large volume fractions (or more closely spaced and fine precipitates) are more

effective in pinning subgrain or grain boundaries. In general, the driving force for recrystallisation (typically 10^7 J m^{-3}) is higher by three orders of magnitude than the Zener "drag" pinning force (typically 10^4 J m^{-3} for reasonably low volume fractions and somewhat coarsened particles). Consequently, small quantities of medium sized to large precipitates on grain boundaries may not have a significant effect on the overall thermodynamics of recrystallisation. If significantly small in size and large in number, however, they do have an effect through their impact on the mobility of the grain or subgrain boundaries.

Analysis of the drag effect by solute or impurity atoms around a moving boundary is more complex than the effect by particles, but that some atom-based drag effect does exist, has been shown often. For instance, many workers[92,114-116] have observed an initial retardation of recrystallisation at high concentrations of solute atoms that was followed by accelerated recrystallisation after the precipitation of the solute atoms into a particle and its subsequent coarsening. Figure 6.9 shows the effect of the solute atoms and their subsequent precipitation and coarsening on recrystallisation i.e. at higher annealing temperatures, recrystallisation precedes precipitation while at lower annealing temperatures there is an interaction between precipitation and recrystallisation and the latter is initially retarded and only accelerates after precipitation and coarsening of the particles. The general condition for the recrystallisation to proceed is, therefore:

$$P_d + P_c > P_z \qquad (6.15)$$

where P_d and P_c are the driving forces due to deformation and precipitation of the second phase given by equations 6.11 and 3.4 respectively and P_z is the retarding force due to Zener drag given by equation 6.14.

In extreme cases of the Zener "drag" effect, the recrystallisation process can completely stop, called "recrystallisation arrest", shown below schematically in the temperature range between T_2 and T_3 for the case of a dislocation density of ρ_2. The Zener "drag" effect can also be manifested by a large deviation of the Avrami exponent n from linearity as shown in figure 6.10.

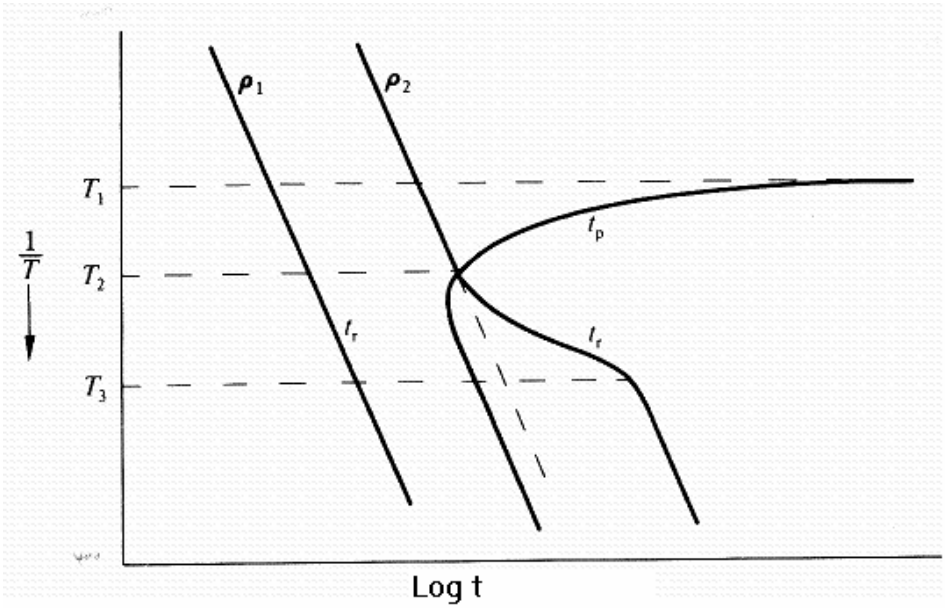

Figure 6.9: The time dependence of the precipitation start time t_p and recrystallisation start time $t_r^{(112)}$.

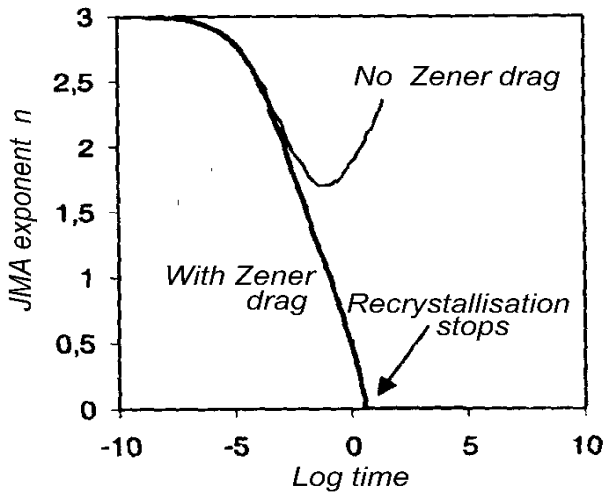

Figure 6.10: The effect of Zener drag on the recrystallisation process as modelled for Ta with oxide particles[117].